

FLOW IN A SOLID-PROPELLANT ROCKET CHAMBER

C.W. Hirt
Flow Science, Inc.
3/1/89

OVERVIEW

Solid propellant rockets involve interesting fluid dynamics problems for several reasons. The burning propellant introduces a time-dependent boundary along which there is a continuous source of mass and energy. Because of this boundary source, special attention must be given to the application of boundary conditions for the interior gas flows. Additionally, flow within a rocket chamber is typically subsonic, while that near the outflow nozzle reaches sonic conditions followed by a supersonic flow in the downstream expansion region of the nozzle. Such diverse flow conditions present a substantial challenge to both experimental and computational modelers

An experimental technique sometimes used for studying flow processes within a rocket chamber is to replace the hot combustion gases with a relatively cold, inert gas. In these so-called "cold flow" tests, gas generated at solid propellant surfaces is modeled by gas injected through a porous wall. The resulting cold, non-reactive environment makes it possible to obtain detailed flow measurements that cannot be duplicated in real rockets.

This note describes a preliminary computational model of a cold flow experiment. The calculation has been performed "blind," that is, without access to the experimental data. To simplify the calculational model, the nozzle region of the rocket chamber was removed and replaced by a specified pressure boundary condition just upstream of the nozzle. A separate calculation made of the nozzle region flow is reported in a supplementary technical note, TN17A.

The principal objective of this note is to show how a two-equation turbulence model alters the internal flow field of a model rocket chamber.

COMPUTATIONAL MODEL

The cylindrical test chamber region to be modeled is 28.5 inches in length and has an internal diameter of 4.0 inches. At

4.55 inches from the closed, rear end of the cylinder there is a radial slot with diameter 7.0 inches and axial thickness 0.40 inches. All interior surfaces, except the closed end of the cylinder and the bottom of the slot, are porous. The computational mesh and obstacles defined to model this arrangement are shown in Fig. 1. Because of axial symmetry, it is only necessary to model one cross section (the axis of symmetry is the left edge of the plotted frames). Concentration of the computational grid near the bottom end of the plots indicates the increased resolution needed to define the small radial slot. In fact, the large aspect ratio of cylinder length to radius makes it difficult to clearly see the slot in the complete obstacle plot.

A steady injection of nitrogen gas is maintained into the chamber through the porous surfaces. The injection speed is assumed to be 29.04 in/s (2.42 ft/s) and is nitrogen gas at a pressure of 30.0 psi and temperature of 500 R. In FLOW-3D this source distribution is defined in terms of obstacle sources. Only mass and energy sources can be defined in FLOW-3D without making code modifications. The momentum of the incoming gas is assumed to be zero; but since this momentum is actually quite small relative to the bulk flow, a zero value is a reasonable approximation.

Initially the chamber was assumed to contain stationary nitrogen gas at 30 psi and 500 R. At the outflow (top) end of the chamber a fixed pressure boundary condition of 30 psi was maintained.

A two-equation, K-Epsilon, turbulence model was included with the usual Navier-Stokes equations. The molecular value of viscosity input for nitrogen was $2.61E-9$ in units of 12 slugs/in/s. Note that a mass unit of 12 slugs is required to have a consistent set of units consisting of inches, seconds, degrees Rankine and pressures in psi. Additionally, the turbulence kinetic energy was initialized to $2.0 \text{ in}^2/\text{s}^2$, and an initial turbulence length scale was set to 0.1 inches. These values are not particularly significant for we shall see that the final level of turbulence energy is many orders of magnitude larger. Boundary conditions for the turbulence model on walls with a gas source require special consideration. This topic is discussed in the next section.

A complete listing of the input file for FLOW-3D is given in Fig. 2. This includes the physical data, computational control data, mesh/obstacle/source data, plus initial and boundary conditions. The input file additionally includes, in Namelist \$GRAFIC, a variety of requests for graphic output. Other graphic output can be obtained with the postprocessor as desired.

TURBULENCE BOUNDARY CONDITONS

Special consideration must be given to the proper boundary conditions to impose on boundaries where there is gas injection. Not only must wall shear stresses be evaluated, but boundary values are needed for the turbulence kinetic energy and turbulence dissipation functions as well.

In the usual two-equation turbulence model, a standard assumption made to arrive at boundary values for the turbulence kinetic energy, q , and dissipation, D , is that near a rigid wall the production of turbulence is exactly balanced by turbulence dissipation. For example, consider a flat wall located at $z=0$ with tangential flow u . Under the above assumption it can be shown that the boundary values for q and D are given by

$$q = - \overline{u'w'} / \sqrt{c_\mu}$$
$$D = - u'w'(\partial u / \partial z),$$

where c_μ is a constant and $\overline{u'w'}$ is the turbulence Reynolds stress.¹⁴ Combining these values with the definition of the turbulence kinematic viscosity in terms of q and D leads to the relation,

$$-\overline{u'w'} = \nu_t (\partial u / \partial z),$$

which shows that the consistency of the turbulence viscosity model is maintained at boundaries.

The problem in using these boundary specifications is that it is first necessary to evaluate the Reynolds stress and the local velocity shear $\partial u / \partial z$. The most common way to accomplish this is to assume a logarithmic law-of-wall velocity profile in which the tangential velocity at a distance z from the wall is related to the shear stress at the wall. Computationally the process is reversed; that is, a velocity computed near the wall is used to evaluate the wall shear stress, which is then used in the equations of motion to advance the velocity and turbulence quantities to a new time.

When there are mass sources at the wall, the usual law-of-the-wall relation cannot be used. In FLOW-3D a modified boundary treatment is used that is based on the following ideas. Assuming

that the boundary is sufficiently flat and that variations in dependent variables along the boundary are small compared to variations normal to the boundary, we can integrate the u-momentum equation from the wall into the flow in the normal (z) direction to obtain,

$$w_s u = -u_*^2 + \nu(\partial u / \partial z) - \overline{u'w'},$$

where w_s is the mass source injection velocity normal to the wall and u_* is the friction velocity at the wall.

It is generally assumed that the viscous stress (second term on the right side) can be neglected away from the wall. Furthermore, w_s is approximately constant according to mass conservation principles, at least to the extent that u is locally independent of position along the wall. Thus, the above relation reduces to

$$w_s u + u_*^2 = -\overline{u'w'}.$$

Schlichting (Boundary Layer Theory, McGraw-Hill Book Co., 1955, Eq. 21.22) has given a solution of this equation using Prandtl's mixing length model for the turbulent stress. The solution is

$$u/u_* = F + (w_s/4u_*)F^2,$$

where the function F is defined by

$$F = (1/\kappa)\ln(zu_*/\nu) + C.$$

Function F contains the von Karman constant $\kappa=0.4$ and an adjustable constant C . For boundaries without a mass source a typical value for C is 5.5. Unfortunately, with mass sources this constant is unknown and must be determined by comparisons with experimental data.

Even if the constant C were known, the above formula relating u_* to u and z is a complicated, implicit relation that is not particularly convenient for numerical purposes. We observe, however, that the presence of w_s has the effect of decreasing the value of the friction velocity because a mass

source reduces the velocity shear at the wall. Thus, if we neglect the influence of w_s on the friction velocity and use the usual logarithmic law-of-the-wall relation to evaluate u_* , we will over estimate its value.

On the other hand, the contribution of u_*^2 to the total shear stress is almost always much smaller than the mass source contribution, so using an approximate value of u_* to compute the total turbulent stress,

$$-\overline{u'w'} = w_s u + u_*^2$$

is not likely to introduce a significant error (particularly in view of the other approximations needed to arrive at this result). Actually, FLOW-3D uses one other approximation as well; the logarithmic expression for u_*^2 is replaced by a (1/7)-power law form for additional computational convenience.

To summarize, then, we shall use a friction velocity computed at walls that neglects the presence of sources and then combine it with the mass source term $w_s u$ to estimate the total turbulent stress. This result is finally used to evaluate the turbulent-function boundary conditions. When there is no mass source the prescription reduces to the usual boundary condition treatment.

COMPUTATIONAL RESULTS

General Remarks

The "cold flow" test, which has no moving boundary corresponding to the burn back of solid propellant, is based on the concept that the burning boundary moves slowly with respect to the gas speed and with respect to the speed of sound in the gas. This slowness means that for a given grain boundary configuration, the resulting gas flow reaches quasi-steady conditions long before the boundary can undergo any significant change. In other words, the complete rocket flow problem can be broken down into the study of a series of quasi-steady problems.

FLOW-3D does not have a specific steady-state option, but computes steady conditions as the limit of a transient solution. Sometimes a transient can be deliberately distorted to increase the rate at which steady conditions are reached. In the present calculation, however, which used a general compressible flow model, no special acceleration techniques were possible. In

particular, uncertainties in what to expect from the effects of turbulence made it necessary to treat the problem as a real transient.

The calculation was run in two parts. The first part carried the problem from an initial, at rest, state out to a time of 0.05 s. A plot showing the history of total mass in the system, Fig. 3, indicates about a 0.9% variation at the end of the calculation. The total energy also exhibited a final variation of 0.9%. The computation took 919 time cycles to reach 0.05 s and required 6.08 hours on a MicroVAX II computer.

Although the total mass and energy were not changing significantly, the average turbulence kinetic energy at 0.05 s still exhibited a variation of about 10%. This was expected because the turbulence distribution depends strongly on diffusive processes that often take more time to settle down. To further improve the steady-state results the problem was restarted and continued on to a time of 0.08 s. This continuation required another 3.53 hours on the MicroVAX II computer. At the end of this continuation the total system mass variation was about 0.5% and the average turbulence kinetic energy variation was down to 1.4%. Pressures in the chamber at 0.08 s only deviated by 0.04% from the average 30 psi values. All of the remaining figures have been made from results at the final 0.08 s time.

Figure 4 displays plots of the turbulence variables for the entire computational region. To compensate for the large aspect ratio of length to radius, which makes visualization of the results difficult, we have enlarged the radial plot coordinate by a factor of 3. Turbulence energy is largest near the chamber wall and increases toward the exit end (top). This is physically reasonable since shear production of turbulence will be greatest at the wall. Also the axial transport of turbulence energy accounts for its accumulation near the exit. Turbulence dissipation shows a similar distribution in agreement with the fact that more turbulence energy implies more dissipation.

Turbulence viscosity, which is proportional to q^2/D , has a somewhat different distribution. The highest value of viscosity is located in the lower right corner of the chamber (see also Fig. 5A). This value appears anomalous since there are similar high values in the bottom corners of the slot. At these locations, in fact, the turbulence energy and dissipation values are low compared to values in neighboring cells. This is due in part to the low flow velocity in these regions. A more important effect, however, is associated with the two perpendicular walls forming the corners. The code thinks the average wall location at a corner is closer than the half width of the cell and this leads to a somewhat higher viscosity than in neighboring cells.

In all cells adjacent to boundaries, the viscosity value is being set by the turbulence boundary conditions, which are dominated by the mass sources in regions of low velocity. A hand calculation indicates that the viscosity induced by mass sources in the present case (i.e., with the present grid resolution of 0.1 inches at the wall) is about $2.38E-6$. It is only in the upper portion of the chamber that velocities are large enough to substantially increase the viscosity along the chamber wall.

If the somewhat anomalous corner values are omitted, the dynamic viscosity has its maximum near the exit end of the chamber in agreement with the maximum of other turbulence quantities in that region. This is shown in Figs. 5A-5E, which contain a collection of "window" plots along the axis of the chamber. These plots offer a considerably clearer picture of the flow. In each subplot of Fig. 5 are shown the turbulence energy, dynamic viscosity and a velocity vector plot.

As the open end of the chamber is approached, the velocity profile exhibits a more pronounced radial profile as well as a rapidly increasing mean velocity. The increase in velocity reflects the increase in integrated mass addition as one proceeds up the axis toward the open end. At the grid location adjacent to the chamber wall there is a rather large velocity indicating the existence of a thin boundary layer that the calculation is not resolving.

The maximum velocity at the exit is 1240 in/s, which corresponds to a Mach number of about 0.09. Because the Mach number is so low, this calculation could have been approximated with an incompressible flow. This result, in fact, shows one advantage of the Implicit-Continuous-Eulerian (ICE) formulation used in FLOW-3D; the time-step size selected by the code for the compressible Navier-Stokes equations was approximately 30 times larger than that possible with an explicit numerical approximation.

There exists very little turbulence energy at the closed end of the chamber because of the low flow velocity in that region. A local maximum in turbulence energy occurs at the opening of the slot where there are relatively large velocity shears generated by the flow coming out of the slot. Downstream of the slot the turbulence energy increases along the chamber wall reaching a maximum at the exit.

The distribution of dynamic viscosity is somewhat different than the turbulence energy. Overall, the turbulence viscosity value is roughly three orders of magnitude larger than the molecular viscosity. A locally high value does exist near the

entrance to the slot and there is a modest increase in magnitude toward the exit end of the chamber. The maximum, however, does not occur at the wall of the chamber where the turbulence energy is maximum. We observe, instead, a maximum value that moves out from the wall, starting at the slot, to a location approximately halfway between the centerline and the wall at the exit plane. On the other hand, the shear stress, which is the product of viscosity and the rate of strain, is probably largest at or near the wall because that is where the rate of strain is largest.

Finally, in Figs. 6-7 there are displayed the computed results for the slot region. Since mass and energy sources on the top and bottom surfaces of the slot are equal, flow distributions within the slot are symmetric with respect to the middle of the slot except near its opening into the main chamber. The presence, in Fig. 7A, of high values of dynamic viscosity in the corners (i.e., locations of two intersecting walls) has already been noted. Leaving out the last column of cells, Fig. 7B, gives a much better picture of the viscosity distribution in the slot. Based on this plot, it is clear that there is a local viscosity maximum just beyond the entrance to the slot.

SUMMARY

The flow in the interior of a model solid rocket chamber has been computed with FLOW-3D. A two-equation turbulence model was employed in the computations using modified boundary conditions to account for wall mass injection. Comparisons with experimental data are clearly needed before any conclusions can be reached as to the accuracy of the computed results. The most critical aspect of the computations is how well the turbulence model, including the boundary condition modifications, can predict the mean turbulence shear stresses.

Some words of caution were noted earlier with respect to the limited numerical resolution of boundary layers. Only through extensive data comparisons will it be possible to assess whether or not the simple turbulence model used here can be relied on for useful engineering analysis. In any case, it has been shown that FLOW-3D provides a convenient platform for performing computational studies of solid propellant rockets.

X-Z MESH

OBSTACLE PLOT

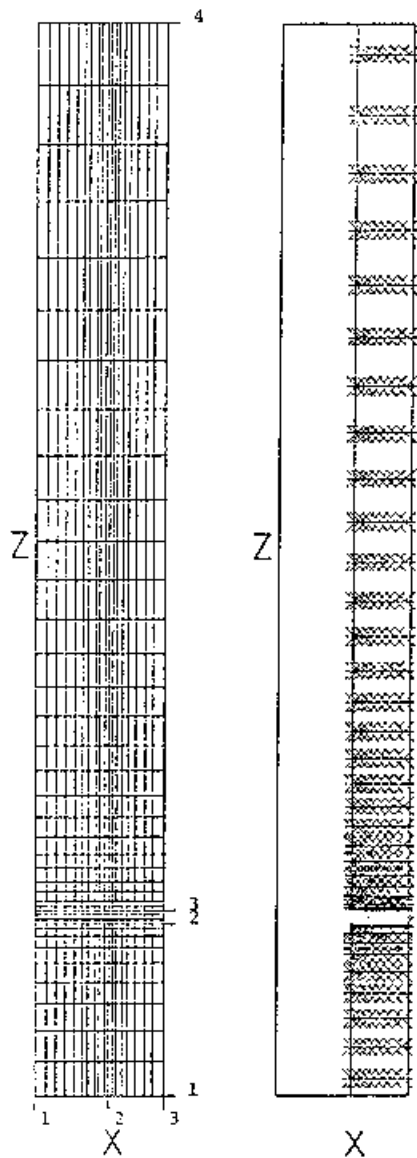


Fig. 1. Mesh (left) and obstacle plot (right).

COLD FLOW - 2

```

INPUT
  ICMPRS=1,      IFVIS=3,      IMSH=1,
  CYL=1.0,      IQSR=2,      IHTC=1,
  WR=2,         WD=2,         HT=5,
  FBCT(1,6)=30., FBCT(1,6)=0.0,  TBCT(1,6)=500.,
  RMHO=1.0,     RHRHO=1.0,  RNK=1.0,
  CV2=9.416E+5, RFD=2.566E+5, MUI=2.61E-9,
  DELT=1.0E-5,  COR=.25,     EPSI=.003,
  TWF=1.0,     PLTDT=.01,    PRDPT=.05,
  TXEL=2.0,     TLEN=0.1,     TREST=.0500056

SEND
SMESH
  NXCELL=16,    FX(2)=2.0,    FX(3)=3.5,    SIZEX(2)=0.1,
  NYCELL=1,     PY(2)=1.83,
  NZCELL=30,    FZ(2)=4.55,    FZ(3)=4.95,  FZ(4)=28.5,
  NZCELL(1)=9,  NZCELL(2)=4,

SEND
SOBS
  NOBS=2,
  IOFO(1,2)=1,  CRXY(1)=-1.0,  CC(1)=2.0,
  IOFO(1,2)=2,  XL(1)=4.95,        QSROBS(1,1)=1.821E-1,
  POBS(1,1)=0.1798E+4, TWOBS(1,1)=0.0,  SAOBS(1)=26.7833,
  IOFO(1,2)=2,  CRXY(2)=-1.0,  CC(2)=2.0,
  POBS(1,2)=2.1112E+4, TWOBS(1,2)=0.0,  SAOBS(2)=6.9148,
  QOBS(1,2)=0.47E-4,

SEND
SYL
  PRESI=30.,

SEND
SBF
SEND
STEMP
  TEMPI=500.,

SEND
SGRATIC
  NVPLTS=3,
  IV1(2)=7,    KV1(2)=9,      KV2(2)=17,
  IV2(3)=11,   KV1(3)=35,
  NCPLTS=5,
  KONTYP(2)=9, KONTYP(3)=10,  KONTYP(4)=10,
  IC1(4)=7,    KC1(4)=7,      KC2(4)=17,
  IC2(5)=11,   KC1(5)=35,
  JLCC(1)=9,   JLCC(1)=2,      XLCC(1)=12,
  JLCC(2)=2,   JLCC(2)=2,      XLCC(2)=23,

SEND
SPARTS
SEND
  
```

Fig. 2. Input data file.

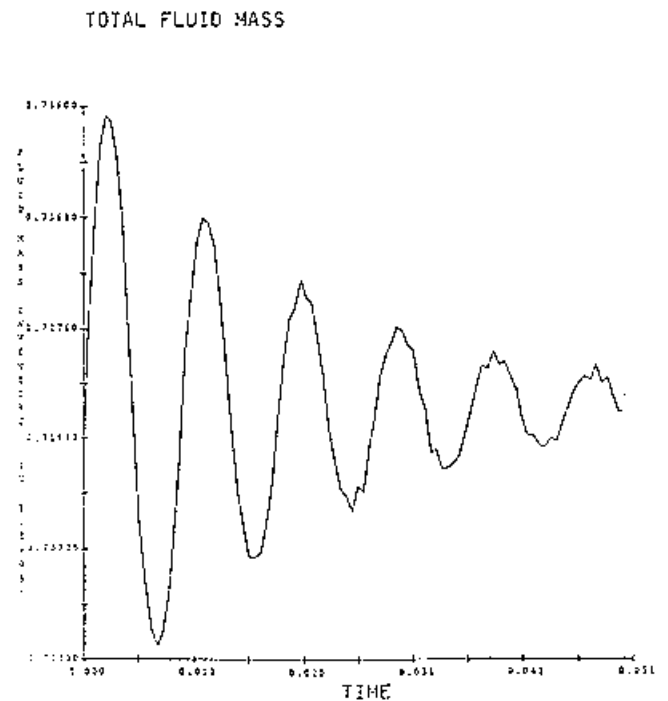
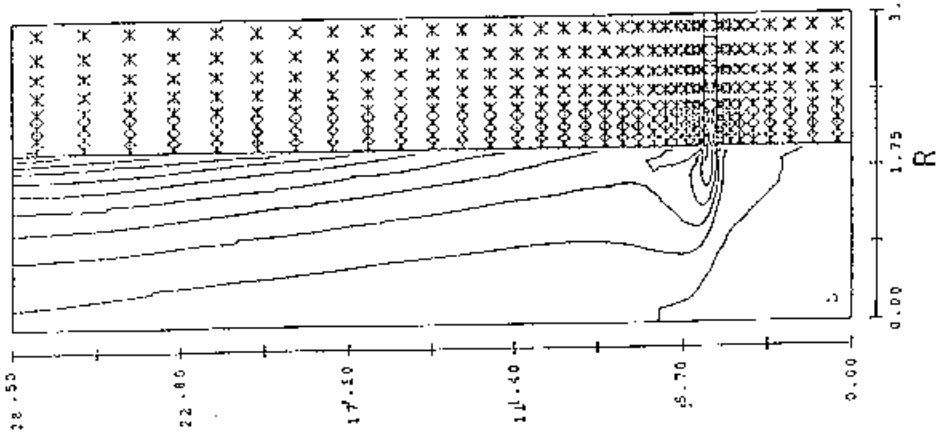


Fig. 3. Total fluid mass history to 0.05 s.

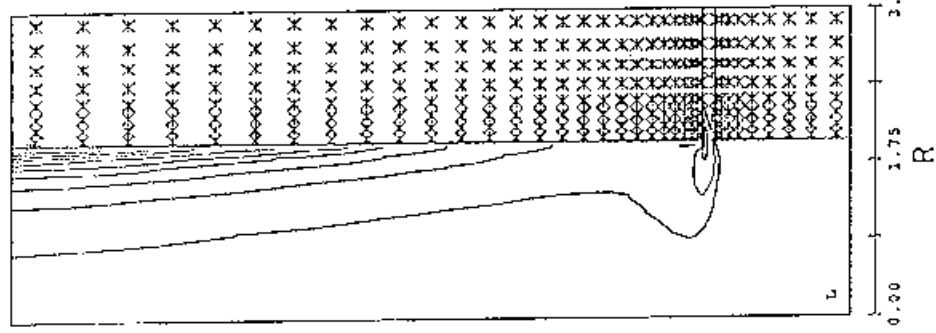
TURBULENT ENERGY CONTOURS

(LOW= 4.565E-01 LOW CONTOUR= 2.627E+03)
 (HIGH= 5.262E+04 HIGH CONTOUR= 4.990E+04)



TURBULENT DISSIPATION CONTOURS

(LOW= 3.050E-01 LOW CONTOUR= 1.130E+06)
 (HIGH= 2.261E+07 HIGH CONTOUR= 2.143E+07)



DYNAMIC VISCOSITY CONTOURS

(LOW= 2.038E-08 LOW CONTOUR= 2.601E-07)
 (HIGH= 4.804E-06 HIGH CONTOUR= 4.563E-06)

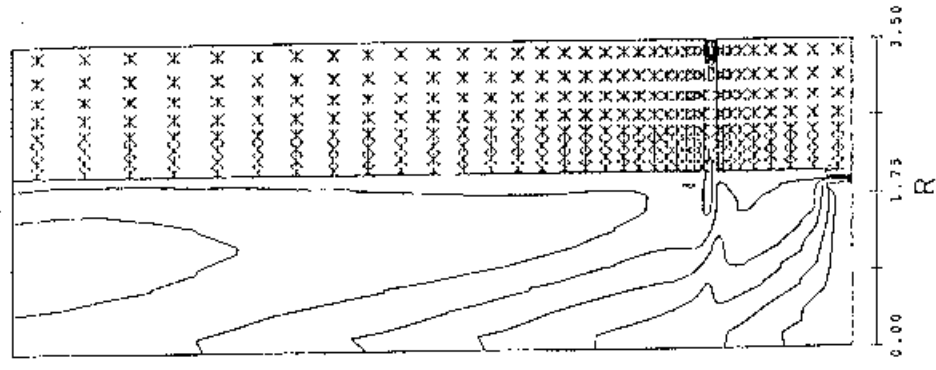


Fig. 4. Contour plots of turbulence quantities in entire chamber. Radial coordinates multiplied by 3.

TURBULENT ENERGY CONTOURS DYNAMIC VISCOSITY CONTOURS VELOCITY VECTORS

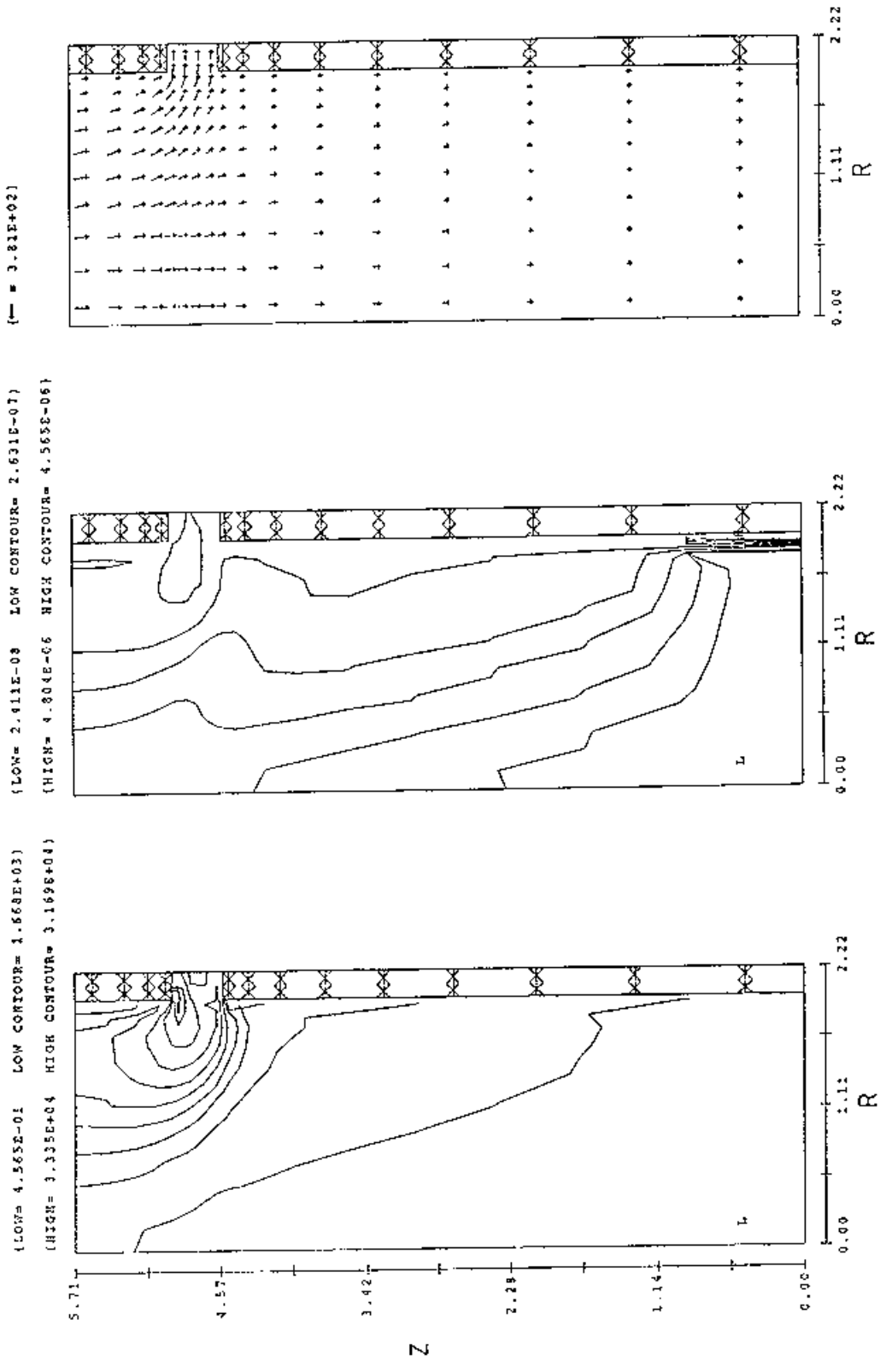


Fig. 5A. Plots in first (lower) 1/5 section of chamber.

TURBULENT ENERGY CONTOURS DYNAMIC VISCOSITY CONTOURS VELOCITY VECTORS

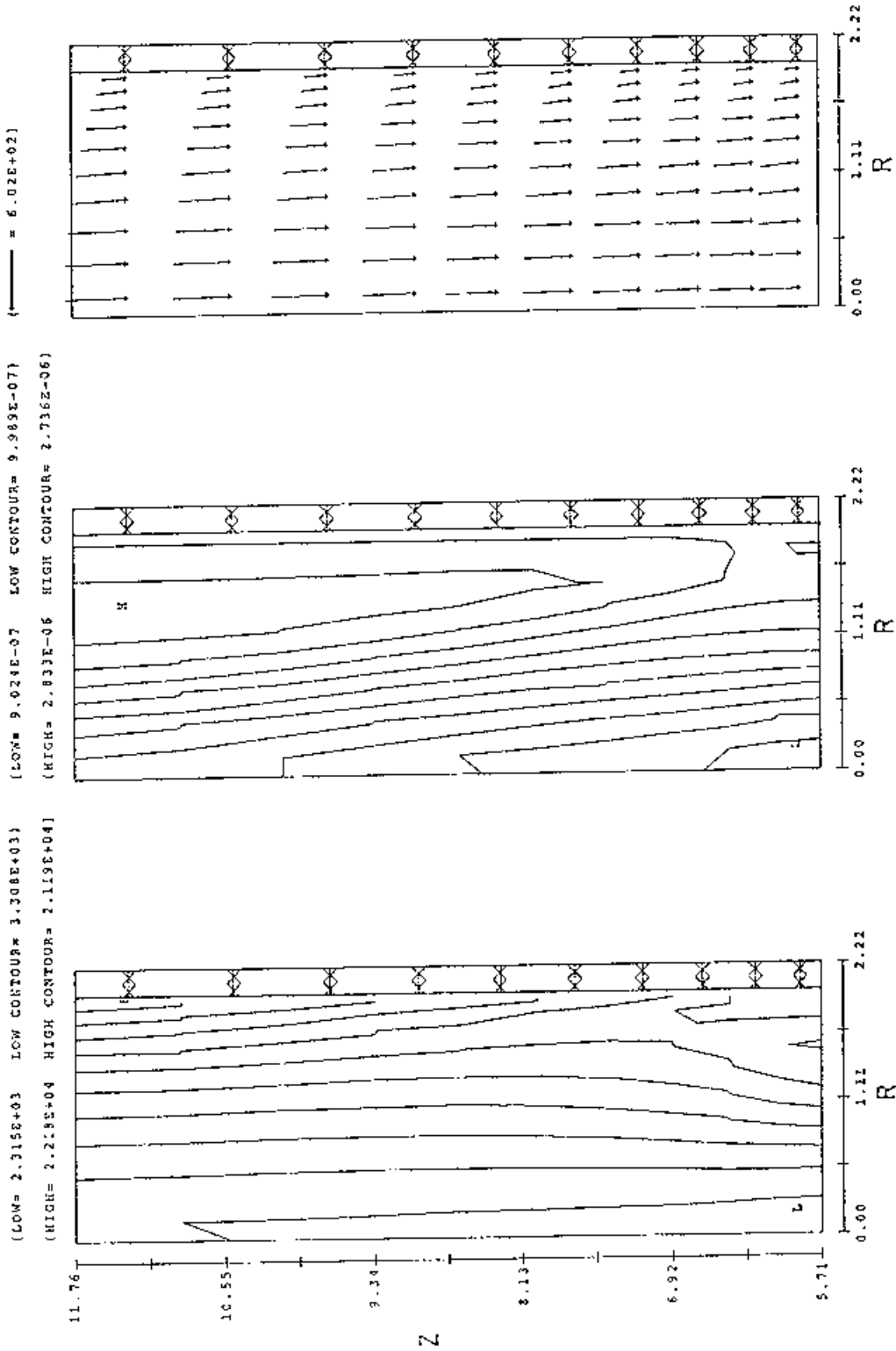
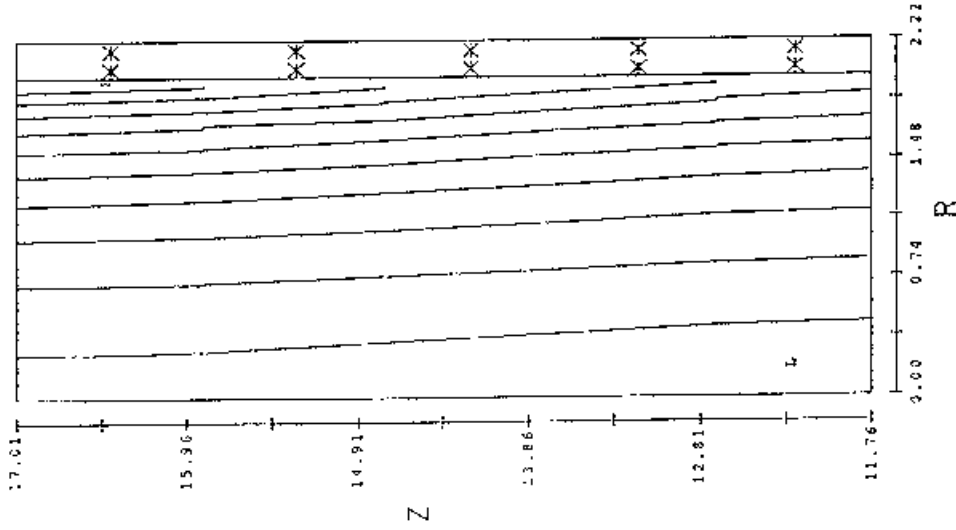


Fig. 5B. Plots in second 1/5 section of chamber.

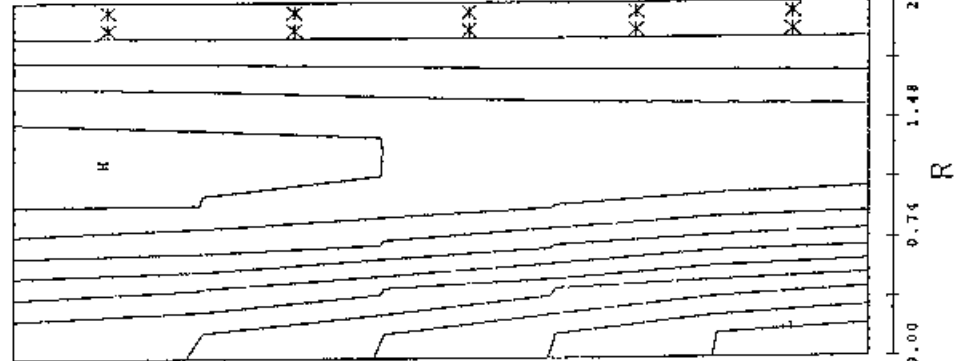
TURBULENT ENERGY CONTOURS

(LOW= 3.624E+03 LOW CONTOUR= 5.074E+03)
 (HIGH= 3.267E+04 HIGH CONTOUR= 3.217E+04)



DYNAMIC VISCOSITY CONTOURS

(LOW= 1.663E-06 LOW CONTOUR= 1.730E-06)
 (HIGH= 2.955E-06 HIGH CONTOUR= 2.891E-06)



VELOCITY VECTORS

(SCALE = 8.10E+02)

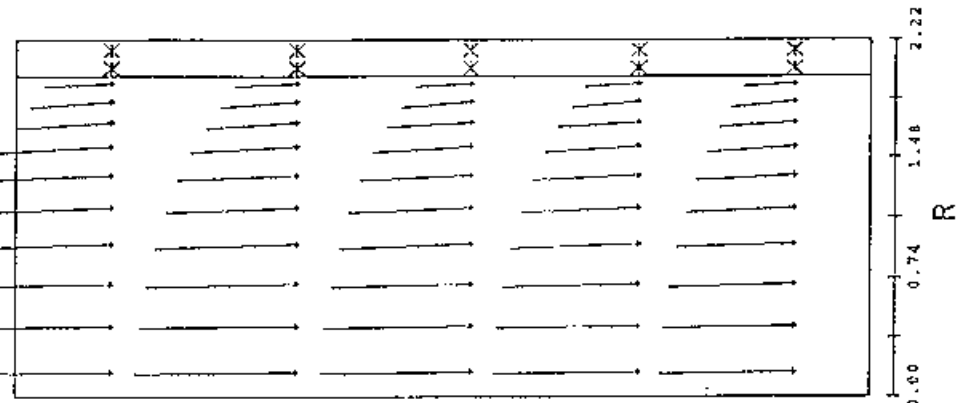
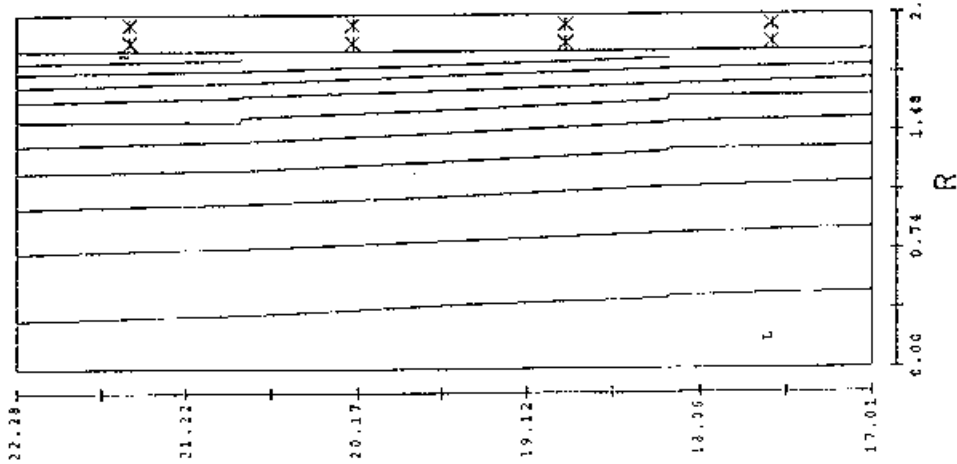


Fig. 5C. Plots in third 1/5 section of chamber.

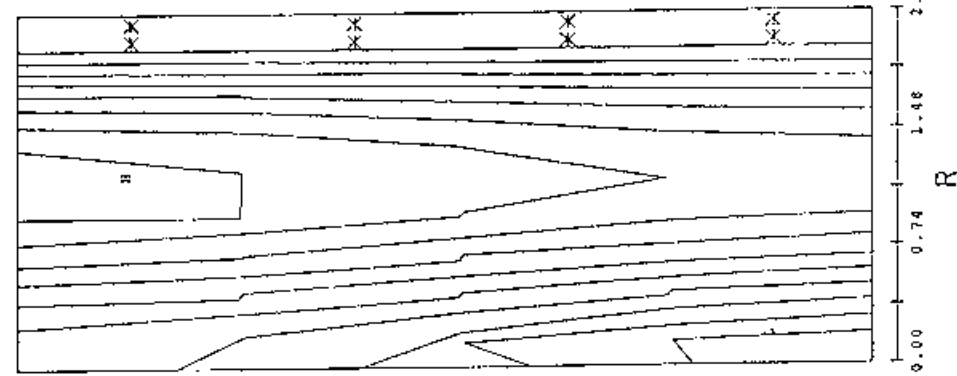
TURBULENT ENERGY CONTOURS

(LOW= 4.775E+03 LOW CONTOUR= 6.619E+03)
 (HIGH= 4.165E+04 HIGH CONTOUR= 3.981E+04)



DYNAMIC VISCOSITY CONTOURS

(LOW= 2.287E-06 LOW CONTOUR= 2.331E-06)
 (HIGH= 3.168E-06 HIGH CONTOUR= 3.124E-06)



VELOCITY VECTORS

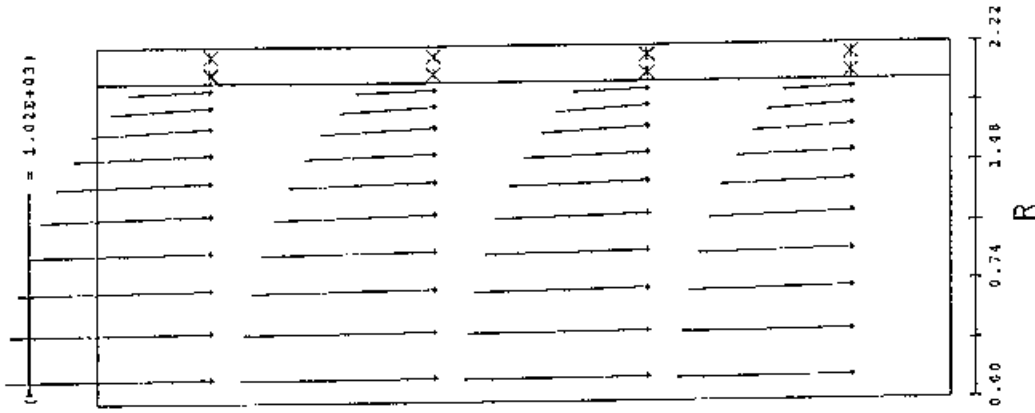


Fig. 5D. Plots in fourth 1/5 section of chamber.

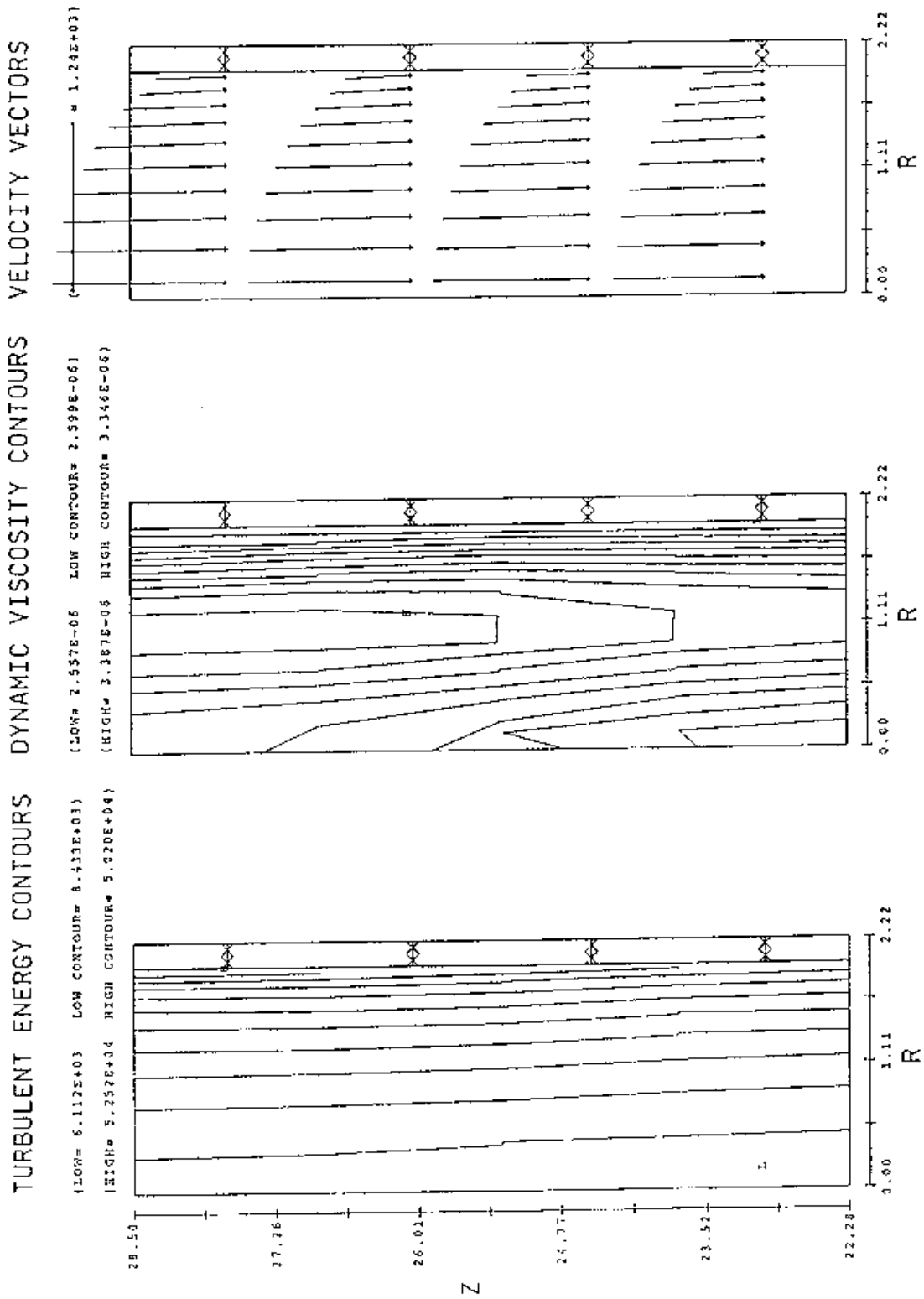
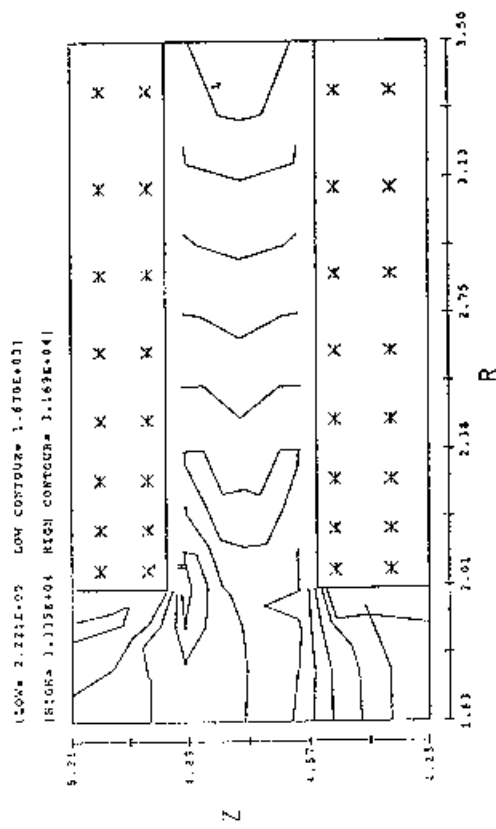
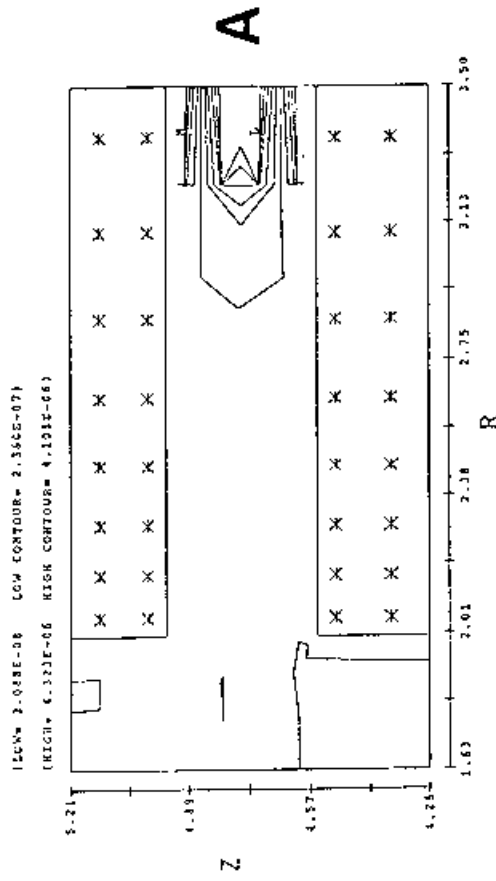


Fig. 5E. Plots in fifth (top) 1/5 section of chamber.

TURBULENT ENERGY CONTOURS



DYNAMIC VISCOSITY CONTOURS



VELOCITY VECTORS

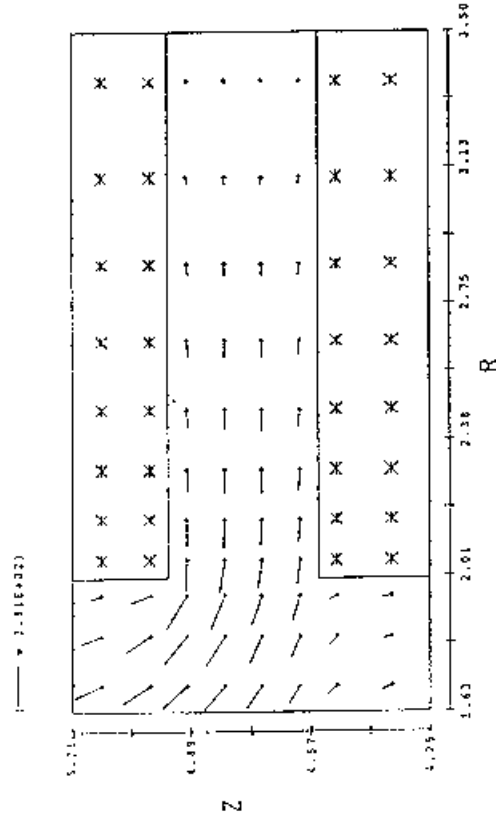


Fig. 6. Computed results in slot region.

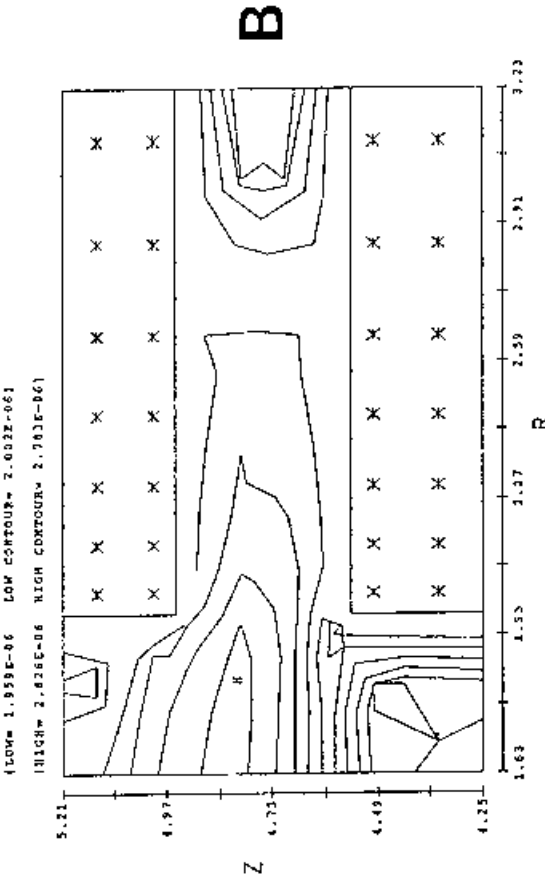


Fig. 7. (A) Turbulence viscosity in slot.
(B) Same as A, but with last column of cells omitted.